Materials Advances

ROYAL SOCIETY OF CHEMISTRY

PAPER

View Article Online
View Journal

Check for updates

Cite this: DOI: 10.1039/d6ma00333h

Evaluation of the influence of various metals in iron-rich acid mine drainage on crystallinity, morphology and textural properties of iron-based MIL-101

Keaoleboga Mosupi,[ab] Christophe A. Ndamyabera,[a] Mike Masukume,[b] L. Scott Blankenship,[c] Robert Mokaya,[c] Nicholas M. Musyoka*[d] and Henrietta W. Langmi*[a]

Received 9th March 2026,
Accepted 11th June 2026

DOI: 10.1039/d6ma00333h

rsc.li/materials-advances

Synthesis of a series of iron-based MIL-101 (MIL = materials institute lavoisier) using iron (Fe) extracted from acid mine drainage waters (AMD) and terephthalic acid extracted from waste polyethylene terephthalate is reported here. Specifically, various metal concentrations that make up AMD are evaluated for their effects on crystallinity, morphological and textural properties of the MOFs. Each metal (Al, Ca, Mg, Mn and Zn) is paired with Fe (dominant metal in AMD) to make bimetallic combinations. Two metals are also paired with Fe to prepare the trimetallic combination series. Generally, MIL-101 was formed with different degrees of crystallinity. Only trace concentrations (<1.25 ppm) of Mg, Mn and Zn were detected, while Al and Ca were undetected in the MOFs, indicating that Fe is the main metal node in all prepared MOFs. The evaluated metals resulted, to some extent in octahedral morphology and/or mixed octahedral and hexagonal bipyramidal of the MOFs. The obtained BET surface areas ranged from 26–2117 $m^2\ g^{-1}$ with the highest pore volume being 0.91 $cm^3\ g^{-1}$. At 77 K and 1 bar, a hydrogen uptake of 1.44 wt% was obtained for MIL-101 from FeMn combination, which also exhibited the highest surface area. This MOF further displayed the highest CO_2 uptake of 6.17 mmol g^{-1} at 298 K and 20 bar. The study proves that at low concentrations, metals within AMD result in MOFs with comparable properties to those derived from pristine precursors. This offers the possibility to use raw AMD directly as precursor for the synthesis of Fe-MOFs, without the need to first extract Fe from AMD.

Introduction

Metal–organic frameworks (MOFs) are materials made of organic linkers coordinated to metal clusters forming materials with open cavities, high surface areas and good thermal stabilities. Although MOFs have such great properties, the industrial application of these materials is predominantly hindered by the high cost of precursors (organic linker and metal salts/oxides). Recycling waste to produce high-value goods is a shared aim, especially in the chemical industry where adopting green chemistry is crucial. The use of waste provides an opportunity to reduce the cost of synthesis thus increasing scaling-up opportunities. Various types of MOFs have been prepared from different types of organic linkers and metal clusters. Metal clusters are commonly derived from particular metal salts, while most common ligands are carboxylates, sulfonates, phosphonate and heterocyclic compounds.[1–3] However, these precursors are often not environmentally friendly and are expensive.

Recent studies have shown that organic linkers such as benzene-1,4-dicarboxylic acid (H_2BDC) can be derived from waste such as textile fibers and waste polyethylene terephthalate (PET) while metal salts can be extracted from spent lithium batteries, coal fly ash and acid mine drainage (AMD).[4–9] The use of waste feedstock has been previously reported to result in almost similar MOF qualities when compared to those prepared from commercial feedstock.[8–10] AMD a byproduct of sulfide mineral oxidation, is a metal rich wastewater that holds promise as a sustainable precursor for the synthesis of iron-based MOFs. AMD, also referred to as acid rock drainage when

---

[a] Department of Chemistry, University of Pretoria, Private Bag X20, Hatfield, 0028, South Africa. E-mail: henrietta.langmi@up.ac.za
[b] Centre for Nanostructures and Advanced Materials, Council for Scientific and Industrial Research (CSIR), Meiring Naude Road, Pretoria, 0001, South Africa
[c] School of Chemistry, University Park, University of Nottingham, Nottingham NG7 2RD, UK
[d] Nottingham Ningbo China Beacons of Excellence Research and Innovation Institute, University of Nottingham Ningbo China, Ningbo 315100, P. R. China. E-mail: nicholas.musyoka@nottingham.edu.cn

formed naturally, primarily results from the oxidation of iron disulfide (FeS_2, pyrite) upon exposure to oxygen and water. This oxidative process occurs in two main stages: initially, pyrite reacts with oxygen and water to yield ferrous iron (Fe^{2+}), sulfate (SO_4^{2-}) and sulfuric acid (H_2SO_4). Subsequently, ferrous iron is further oxidized to ferric iron (Fe^{3+}), which hydrolyzes to form brownish-red ferric hydroxides ($Fe(OH)_3$) and releases additional acidity.[11] While this geochemical process can occur naturally over geological timescales, anthropogenic activities, particularly mining and mineral extraction, significantly accelerate the rate and volume of acid generation due to increased exposure of sulfide minerals. AMD is ecologically hazardous, typically exhibiting a low pH and high concentrations of iron, aluminum, manganese, calcium, magnesium and various toxic heavy metals such as arsenic, lead and cadmium.[12,13]

The precipitation of metal ions from AMD can be achieved through alkaline treatment, wherein agents such as lime ($Ca(OH)_2$) or sodium hydroxide (NaOH) are introduced to raise the pH and facilitate the formation of metal hydroxides.[14] This method not only provides an effective remediation route for AMD but also offers a cost-efficient and scalable strategy for recovering iron and other valuable metals, which may be repurposed for the synthesis of iron-based MOFs or other advanced materials.

Structurally, Fe-MOFs such as MIL-101 exhibit high specific surface areas and large pore volumes, both of which are essential for maximizing physisorption of hydrogen. Additionally, the presence of open Fe^{3+} metal sites enhance the interaction energy with H_2 molecules, thereby improving the adsorption capacity at cryogenic and near-ambient temperatures.[15–17] The frameworks also exhibit a good thermal and chemical stability, essential for repeated adsorption–desorption cycles. These properties make Fe-MOFs a promising class of materials for solid-state hydrogen storage systems aligned with clean energy objectives.

This study investigates the synthesis of MIL type MOFs, specifically Fe-MIL-101, consisting of trivalent iron (Fe^{3+}) oxo-clusters and the ditopic carboxylate linker, 1,4-benzenedicarboxylic acid (H_2BDC). The Fe^{3+} ions are selectively recovered from AMD through alkaline precipitation, while H_2BDC is sustainably derived from waste PET, offering a low-cost and environmentally friendly approach to MOF synthesis. Beyond single-metal systems, this work extends to a comprehensive evaluation of the influence of additional metals commonly present in AMD (namely Al, Mg, Ca, Mn and Zn) on the synthesis and structural properties of the iron-based MOFs. Binary (Fe–M) and ternary ($Fe–M_1–M_2$) metal combinations are prepared in representative molar ratios reflective of their natural abundance in AMD, to explore their impact on the crystallinity, morphology, porosity and surface area of the resulting frameworks.

Fe-MIL-101 frameworks impose strict geometric and charge requirements on any additional metal incorporation; therefore, metals such as aluminum and manganese might partially substitute Fe(III) and result in mixed-metal nodes under controlled synthesis. In contrast, divalent metals such as Mg, Ca and Zn typically substitute at defects sites, coordinate with ligands or deposit on the surface because of charge and size disparity. Fig. 1 shows metal cluster mixture, partial substitution or surface deposition of various metals.

To the best of our knowledge, this is the first study to systematically assess the effect of AMD-associated coexisting

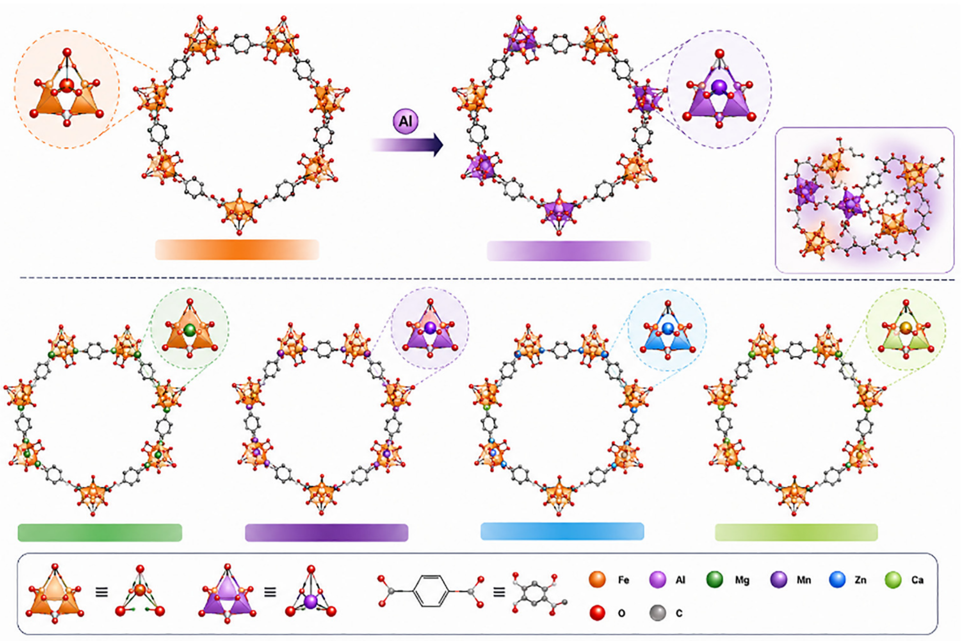

Fig. 1 A schematic representation of metal incorporation and/or partial substitution of various metals into Fe-MIL-101 framework (generated using ChatGPT OpenAI (05/05/2026)).

metal ions on the synthesis and physicochemical characteristics of Fe-based MOFs. The findings contribute valuable insights toward the development of MOFs from industrial wastewater sources and broaden the understanding of multi-metallic system behavior in MOF formation.

The chemical composition of surrounding solution in Fe-MOF synthesis can easily influence the redox and coordination environment of iron clusters. Recent reports have shown synthesis parameters, starting material composition and metal speciation significantly affect crystallinity, porosity, morphology and stability of Fe-MOFs.[18] However, most studies are performed under simplified laboratory conditions employing high-purity precursors, while the influence of complex multi-metal systems such as AMD remains insufficiently understood. Combination of various metals could reveal how competitive coordination, ionic strength and redox interactions affect nucleation and crystal growth, consequently affecting phase formation, defect density and particle size distribution. The role of foreign metal ions during framework assembly has received limited attention despite its critical role in ecological implementations. Since AMD composition is often determined by the surrounding geological conditions, studying the variability of these elements could indicate the potential to synthesize Fe-MOFs from any AMD source, as long as it is rich in Fe (especially given that circumneutral AMD waters also exist). This study can potentially shift the paradigm from purified systems to real-world aqueous matrices; this approach could potentially open doors for scalable production of functional Fe-MOFs while simultaneously contributing to sustainable waste management.

Experimental

Materials and reagents

Aluminum chloride hexahydrate ($AlCl_3{\cdot}6H_2O$, 99%), zinc nitrate monohydrate ($Zn(NO_3)_2$), ethylene glycol ($HOCH_2–CH_2O$, 99.8%), sodium hydroxide (NaOH pellets) were obtained from Sigma-Aldrich. Hydrogen peroxide (H_2O_2, 50%), magnesium nitrate hexahydrate ($Mg(NO_3)_2{\cdot}6H_2O$, 98%) and manganese sulphate monohydrate ($MnSO_4{\cdot}H_2O$, 98%) were procured from Associated Chemical Enterprises. Calcium nitrate tetrahydrate ($Ca(NO_3)_2{\cdot}4H_2O$, 99%), ethanol (CH_3CH_2OH, 99.9%), glacial acetic acid (CH_3COOH, AR), hydrochloric acid (HCl, 32%) and *N*,*N*-dimethylformamide (DMF, 99.8%) were purchased from Radchem. Deionized water was obtained from Milli-Q® SQ 2series Lab Water Systems Work. AMD water was sourced from a mine in Mpumalanga, South Africa and PET waste bottles were collected from domestic waste in the Gauteng province, South Africa.

Fe-MIL-101 synthesis

The extraction of iron from AMD and H_2BDC from PET was reported elsewhere.[10,19] All the MIL-101 MOFs were synthesized using AMD-Fe and PET-BDC as precursors. In a typical procedure, 1 g of AMD-Fe (with some trace amounts of other metals (see Table 2) was dissolved in 5 mL HCl, followed by the addition of a specific amount of various metal salts to adjust the concentration of coexisting metals naturally present in AMD, thereby generating bimetallic and trimetallic combinations as outlined in Table 1. In a separate beaker, 1 g of PET-BDC was dissolved in 50 mL DMF. The two solutions were transferred into a Teflon-lined autoclave, placed in a conventional oven and heated at 110 °C for 20 h. The red precipitate formed was then collected by centrifugation, and thereafter, washed with DMF and hot ethanol twice, respectively. The sample was then dried at 60 °C under vacuum overnight.

MIL-88B was also prepared in a similar manner as proof of concept (see SI).

Characterization

The composition of prepared MOFs was analyzed using Agilent 4210 MP-AES instrument. Crystallinity of the samples was determined using a PANalytical X'Pert Pro powder diffractometer fitted with a Pixcel detector. This equipment employs a Ni-filtered Cu-Kα radiation (0.154 nm). The scanning rate was set at 0.2° s^{-1} and patterns were obtained in a 2θ range of 3–40°. The coordination of the organic linker to the metal clusters was

Table 1 Amounts of various metal salts (g) used in the synthesis of the MOFs. The molar ratios are in brackets (Fe normalized to 1)

Bimetallic combination						
Metals	AMD-Fe	$AlCl_3{\cdot}6H_2O$	$Ca(NO_3)_2{\cdot}4H_2O$	$MnSO_4{\cdot}H_2O$	$Mg(NO_3)_2{\cdot}6H_2O$	$Zn(NO_3)_2$
FeAl	1.0000	0.0830 (0.031)	—	—	—	—
FeCa	1.0010	—	0.1291 (0.049)	—	—	—
FeMg	1.0120	—	—	0.1114 (0.058)	—	—
FeMn	1.0090	—	—	—	0.0225 (0.008)	—
FeZn	1.0223	—	—	—	—	0.0023 (0.001)
Trimetallic combination						
Metals	AMD-Fe	$AlCl_3{\cdot}6H_2O$	$Ca(NO_3)_2{\cdot}4H_2O$	$MnSO_4{\cdot}H_2O$	$Mg(NO_3)_2{\cdot}6H_2O$	$Zn(NO_3)_2$
FeAlCa	1.0110	0.0830 (0.031)	0.1252 (0.047)	—	—	—
FeAlMg	1.0211	0.0832 (0.030)	—	0.1056 (0.041)	—	—
FeAlMn	1.0100	0.0838 (0.031)	—	—	0.0235 (0.009)	—
FeCaMg	1.0013	—	0.1212 (0.046)	0.1086 (0.040)	—	—
FeCaMn	1.0002	—	0.1251 (0.047)	—	0.0248 (0.009)	-
FeCaZn	1.0056	—	0.1244 (0.047)	—	—	0.0025 (0.001)
FeMgMn	1.0002	—		0.1015 (0.040)	0.0231 (0.009)	—
FeMgZn	1.0531	—		0.1172 (0.045)		0.0028 (0.001)

evaluated using a JASCO FT/IR-4X Fourier transform infrared (FTIR) spectrometer. Spectra were collected between 4000 to 450 cm^{-1} using a resolution of 4 cm^{-1}. Before the analysis, a background scan was run. Morphology of the prepared MOFs was determined using a JEOL-JSM 7500F scanning electron microscope (SEM). Prior to analyses samples were coated with carbon. Metal analysis of the prepared MOFs was determined using an Agilent 4210 microwave plasma-atomic emission spectrometer (MP-AES) calibrated with a multielement standard. Thermal decomposition of the materials was evaluated using a Mettler Toledo, TGA/SDTA 851e instrument. 10 mg of sample was gradually heated to 900 °C at a rate of 10 °C min^{-1} under inert conditions.

N_2 and H_2 (99.999% purity) isotherms at 77 K and up to 1 bar were acquired using a Micromeritics 3flex analyzer. All sample masses were measured using a microbalance with a resolution of 0.1 mg, minimal sample mass used was 200 mg. Freespace measurements were made at ambient and analysis temperatures using He (99.999% purity) and used by the instrument software to perform the conversion of the isotherm to ''total'' adsorption. Textural characteristics were calculated by deconvolution of N_2 isotherms. BET areas were calculated based on the Rouquerol criteria. Pore volume was calculated at a relative pressure of 0.9. Average pore width, $w_{avg} = 4V/A$ was determined by assuming cylindrical pores. Micropore volume was determined using *t*-plot method employing the Hakins and Jura thickness equation/(Dubinin–Radushkevich). Barrett–Joyner–Halenda (BJH) method was applied to obtained pore size distributions. Prior to all analyses, the MOF samples were degassed by heating at 150 °C under vacuum for 12 h using SmartVac degassing system.

CO_2 measurements were conducted at 298 ± 1 K and up to 20 bar using a Hiden Intelligent Gravimetric Analyzer (IGA). Prior to CO_2 adsorption measurements, the MOF samples were outgassed by heating at 150 °C under vacuum. Mass measurement precision of the IGA is 0.1 μg with a mass stability of 1 μg, dry sample mass was >30 mg for all samples. The instrument provided a pressure precision of 0.02% for each isotherm point and a base vacuum pressure of below 1×10^{-6} mbar. For each isotherm point, equilibrium uptake was determined by identifying the asymptote of rate of change in uptake following 99% relaxation, with a tolerance of 2%. Equilibration data was acquired every 1 s. Instrument software automatically converts the isotherm to absolute, using the input skeletal density of the adsorbent, and the gas and liquid densities of the adsorbate. Skeletal densities were determined using a Micromeritics Accupyc II.

Results and discussion

Powder X-ray diffraction (PXRD)

Fig. 2 presents the PXRD patterns for bimetallic MIL-101 (Fig. 2a) and trimetallic MIL101 (Fig. 2b). The PXRD patterns show the majority of samples displaying sharp peaks at 2θ of 8.5°, 9.2° and 17.1°. The small areas under the peaks indicate that materials are highly crystalline except the FeAl-MIL-101 sample which is characterized by broad peaks between 8.5° and 9.2°, which is indicative of an amorphous material. The FeAl-MIL-101 combination yielding amorphous MOF materials has been reported by Kulandaivel *et al.*[20] The amorphization of this material is not only due to loss of crystallinity but also to shift in the balance of nucleation, trinuclear metal–oxo formation and long-range framework proliferation due to Al addition.[21] Even though Fe^{3+} and Al^{3+} are isovalent, the secondary building unit and stability are perturbed by Al's smaller ionic radius and higher charge density, introducing local lattice strain, and changing M–O distances encouraging metal compositional heterogeneity as hydrolysis rates diverge.[22] Incorporation of Al kinetically decouples ordered framework assembly, inducing defect-rich, poorly correlated networks over periodic crystals, an occurrence echoed in MOFs where accumulation of defects leads to amorphization.[23] A high number of

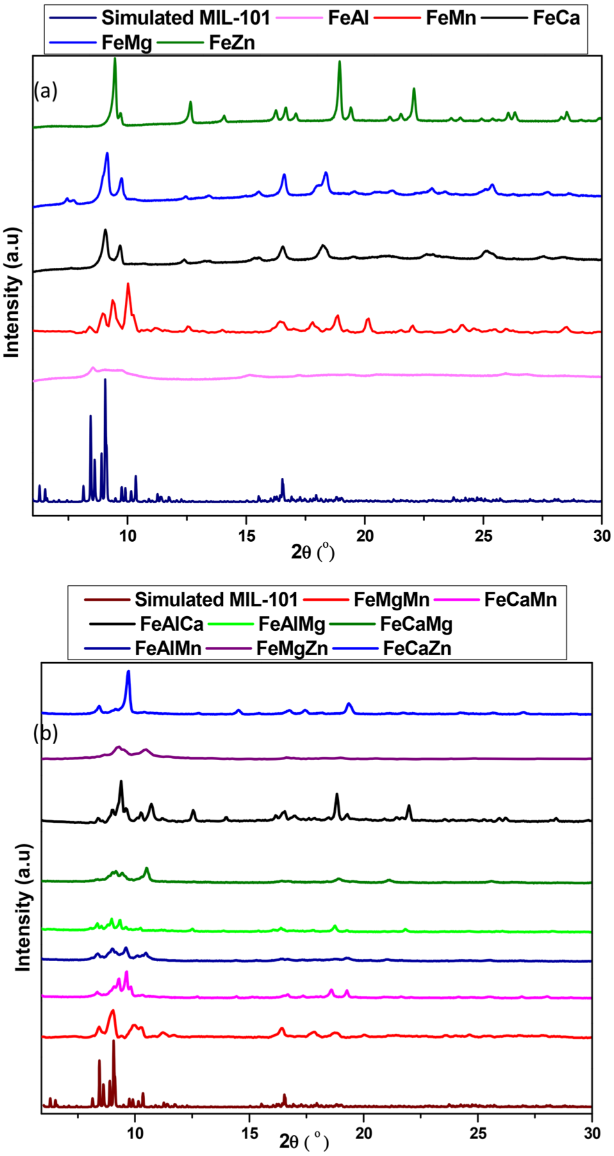

Fig. 2 Powder X-ray diffraction patterns for MIL-101 synthesized from (a) bimetallic and (b) trimetallic combinations.

defects such as missing linkers, missing-cluster or disordered node formation disrupts metal–ligand coordination and destroys long range order, this is likely exacerbated by Al geometric mismatch and altered coordination kinetics, directing crystallization to an amorphous material.[24] FeMn-MIL-101 sample displayed an additional peak at 10.1° which is indicative of the co-existence of both MIL-88B and MIL-101 as previously reported.[25,26] FeMn-MIL-53 has been reported before and the report suggested that Mn(II) could not directly coordinate with BDC but could enable the isomorphic substitution of partial Fe(III).[27] The structural features of MIL-type MOF is not highly affected by the inclusion of Mn. MIL-type systems form through trinuclear μ_3-oxo clusters (Fe_3O units) that forms through rapid hydrolysis of Fe(III) and strong Fe–O bonding. The lower charge density and slower hydrolysis kinetics of Mn(II) typically favor mononuclear or less strongly connected systems. Sun *et al.* prepared FeMn MOFs and for all samples, the PXRD patterns showed only a slight decrease in peak intensities with no evidence of discrete manganese species since no peaks belonging to any manganese species (manganese oxides or manganese salts) were found.[28] This was attributed to partial isomorphic substitution of Fe by Mn atoms. FeZn-MIL-101 displayed highly intense peaks with small regions under the peaks which is indicative of high crystallinity. PXRD patterns displayed a highly crystalline MIL-53 MOF, which indicated that the inclusion of Ca(II) does not cause disorder to the primary topology of the MIL-type MOF.[29] It is evident that, divalent metals have little to no effect on the morphology or crystallinity of MIL-101 MOF.

Majority of the trimetallic combination displayed an additional peak at 2θ above 10° which is similar to what is observed for FeMn-MIL-101 samples. FeMgZn-MIL-101 and FeCaMg-MIL-101 samples displayed two peaks that are broad and of low intensity, which indicates moderate crystallinity of the sample. The FeAlCa-MIL-101 and FeCaZn-MIL-101 displayed good crystallinity as indicated by high intensity peaks relative to other samples. Overall, the prepared materials displayed a reasonable degree of crystallinity, although some materials suffered from mixed phases and some ended up more amorphous.

Fourier transform infrared spectroscopy (FTIR)

FTIR spectra for all samples are presented in Fig. 3. For all the synthesized bimetallic and trimetallic MOFs, the prominent bands at 1390 and 1597 cm^{-1} are attributed to ν_{as}(COO) and ν_s(COO) vibration bands, which are characteristic absorption bands of carboxylate. The vibrational band at 1659 cm^{-1} is assigned to C═O stretching. The weak bands at 1050 and 750 cm^{-1} are assigned to C–H bending vibrations of the benzene ring. The coordination of the carboxylate to the metal cluster (Fe–O) is confirmed by the absorption band at 550 cm^{-1}. The results obtained are similar to previous reports.[30,31] These results show that the prepared MOFs contain the deprotonated organic linker. Additionally, there is no apparent shift of the Fe–O band, which is normally observed for bimetallic or substituted MOFs.[32,33] C═O shift to high wavenumber observed by Duan *et al.*, due to competing effects of metalation, was not observed in this study.[34] This then confirms that the added metals did not form part of the MOF structure. All the prepared samples (bimetallic and trimetallic combinations) displayed very similar bands.

Microwave plasma atomic emission spectroscopy (MP-AES)

MP-AES was used to determine the presence of other metals besides iron in the structure of the MOFs. Table 2 shows iron concentrations acquired at 344.06 and 371.99 nm, as well as concentrations of additional metals obtained at their characteristic wavelengths (Mg at 285.21 nm, Mn at 403.08 nm and Zn at 472.21 nm). Multiple wavelength are used by MP-AES to overcome spectral interferences and accommodate a wide linear dynamic range. The equipment was calibrated using known standards of 1, 5, 10 and 20 ppm prior to analysis. Al, Ca and Zn were undetected from all samples hence excluded from Table 2. The results obtained show that MOFs are mainly made of iron metal with minor contributions from other metals. All the prepared samples displayed an average concentration between 11–15 mg L^{-1} of iron from a 100 mg L^{-1} sample. Samples such as FeMg-MIL-101, FeCaMn-MIL-101, FeMgZn-MIL-101 and FeAlMg-MIL-101 displayed minor concentrations corresponding to Mn

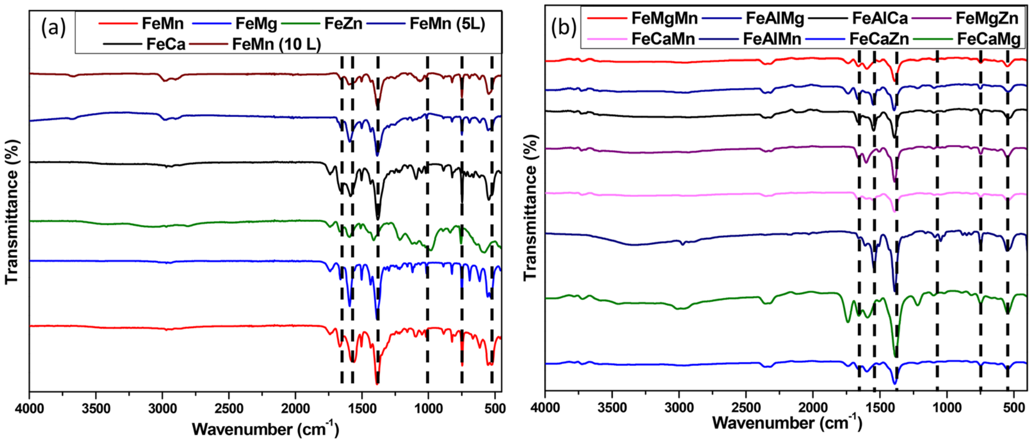

Fig. 3 Fourier transform infrared spectra for MIL-101 synthesized from (a) bimetallic and (b) trimetallic combinations.

Table 2 Metal concentrations (ppm) in the as-synthesized MOFs measured at corresponding emission wavelengths by microwave plasma–atomic emission spectroscopy (MP-AES)

Solution label	Fe	Fe	Mg	Mn	Zn
Blank	0	0	0	0	0
1 ppm	1	1	1	1	1
5 ppm	5	5	5	5	5
10 ppm	10	10	10	10	10
20 ppm	20	20	20	20	20
Blank	0.19	0.17	0.04	0.02	0.05
AMD-Fe	29.38	30.49	0.13	0.08	0
FeMn	15.84	15.85	0	0.06	0
FeMg	11.6	11.61	0	0.02	0.07
FeZn	15.79	16.07	0	0.08	0
FeCa	12.59	12.73	0	0	0.05
FeMgMn	16.99	17.23	1.23	0.03	0.05
FeAlMg	12.8	12.82	0.12	0	0.07
FeAlCa	11.8	11.99	0.11	0.02	0.07
FeMgZn	13.24	13.37	0.83	0	0
FeCaMn	12.89	13.19	0	0.22	0.05
FeAlMn	12.23	12.18	0.49	0	0
FeCaZn	14.25	14.15	0.2	0.04	0.08
FeCaMg	12.51	12.97	0.99	0.03	0.05

and Mg. However, the concentration of these metals did not exceed 1.25 ppm. For example, the highest detected Mg concentration was 1.23 ppm for FeMgMn-MIL-101 sample while the highest for Mn was 0.22 ppm for FeCaMn-MIL-101 sample, respectively. The obtained low concentration of additional metals, relative to iron, indicates that iron is the main metal node in all prepared materials. The low or absence of additional metals indicates that these species are only present as dopants or surface-associated species, rather than as structural metal centers in the MOF structure. The absence, especially of divalent metals, could be attributed to the fact that Fe^{3+} often display strong affinity for carboxylate linkers. Although the synthesis of FeMg/Zn-BDC has been reported before (MgFe-BDC was amorphous while FeZn-BDC displayed spindle-like morphology), their low concentration in this study hindered their incorporation in the MOF structures.[35] Ca and Mg are more difficult to incorporate into mixed MOF nodes with Fe due to their inherent weak coordination, propensity to form non-redox sites and often larger ionic radii.[36–38] It is also challenging to incorporate Mg into Fe clusters due to difference in charge density in addition to the fact that, Fe forms stable oxo-clusters while Mg prefers simpler octahedral aqua complexes. If Mg is found in MIL-101 structure, it might be attached on the surface of the organic linker *via* carbonyl interaction. It is very challenging to prepare mixed metal MOFs in a one-step synthesis because the incorporation of secondary and tertiary metal nodes into MOF structures tends to form erratic topologies and functions.[39]

Scanning electron microscopy (SEM)

SEM was used to visualize the surface morphology of the materials and the results are presented in Fig. 4 and 5. The majority of the bimetallic combination samples displayed the octahedral morphology associated with MIL-101 (Fig. 4). The MOF from FeAl-101 combination displayed no distinct crystal facets or shapes associated with MIL-101, suggesting that the material is amorphous in agreement with the PXRD pattern (Fig. 2a). MIL-101 from FeMg combination displayed both octahedral and hexagonal bipyramidal morphology. FeMn-MIL-101, FeCa-MIL-101 and FeZn-MIL-101 particles are intermingling with irregular shaped particles. The trimetallic combination MOFs exhibited a similar morphology to the bimetallic combination MOFs (Fig. 4). However, the MOFs synthesized from the FeMgMn and FeAlMg combinations demonstrate the octahedral structures intermingling with irregular rod-like shapes (Fig. 5a and b). The FeCaMg combination MOF sample displayed a mixture of octahedral and hexagonal bipyramidal morphology (Fig. 5h). The appearance of the hexagonal bipyramidal morphology, which is mostly associated with MIL-88B, in MIL-101 synthesis has been reported.[40] The occurrence of this combination of morphologies is as a result of the acidic environment brought about by the dissolution of AMD-Fe. The acidic environment promotes the formation of thermodynamically stable phase MIL-88B in combination with the kinetically stable phase MIL-101.[41,42] The octahedral particles with smooth surface correspond well to previous reports.[43–46] It can be observed that the particle sizes of bimetallic combinations are larger than the trimetallic combinations (see particle size distribution plots (Fig. 4f–i and 5i–p)). The average particle size distribution of trimetallic combination might be increased by the presence of large hexagonal bipyramidal crystal, especially for FeCaMg (Fig. 5h and p). The heterogenous and large distribution of particle size is often reported for MIL-101 material.[47,48] The difference can be attributed to nucleation and growth rates, since kinetics of crystal formation can be sensitive to reaction environment. The trimetallic combination MOFs may slow down or terminate crystallization early, by possibly altering ligand binding strength, resulting in small crystals.[49] The trimetallic combination is highly supersaturated as compared to bimetallic combination which results in small crystal sizes.[50]

Transmission electron microscopy

Fig. 6 displays TEM images of selected bimetallic and trimetallic combinations (based on high surface area and better gas adsorption). The obtained samples displayed octahedral morphology comparable to the one observed in SEM images. FeMgMn and FeAlMg octahedral particles intermingle with rod-like particles as observed in SEM images (Fig. 5a and b). The particles displayed some rough surfaces which had been reported before.[51–53]

Thermogravimetric analysis

The thermal degradation of MOF samples was examined using TGA. Fig. 7a and b show the TGA profiles of bimetallic and trimetallic samples, respectively. The plots display a bimodal mass loss which is commonly associated with iron-based MOF structures. The initial mass loss (5–30%) at temperatures below 150 °C is ascribed to loss of moisture and/or solvents molecules trapped within the cavities and/or interacting with open metal sites. The bimetallic combination MOFs displayed varying

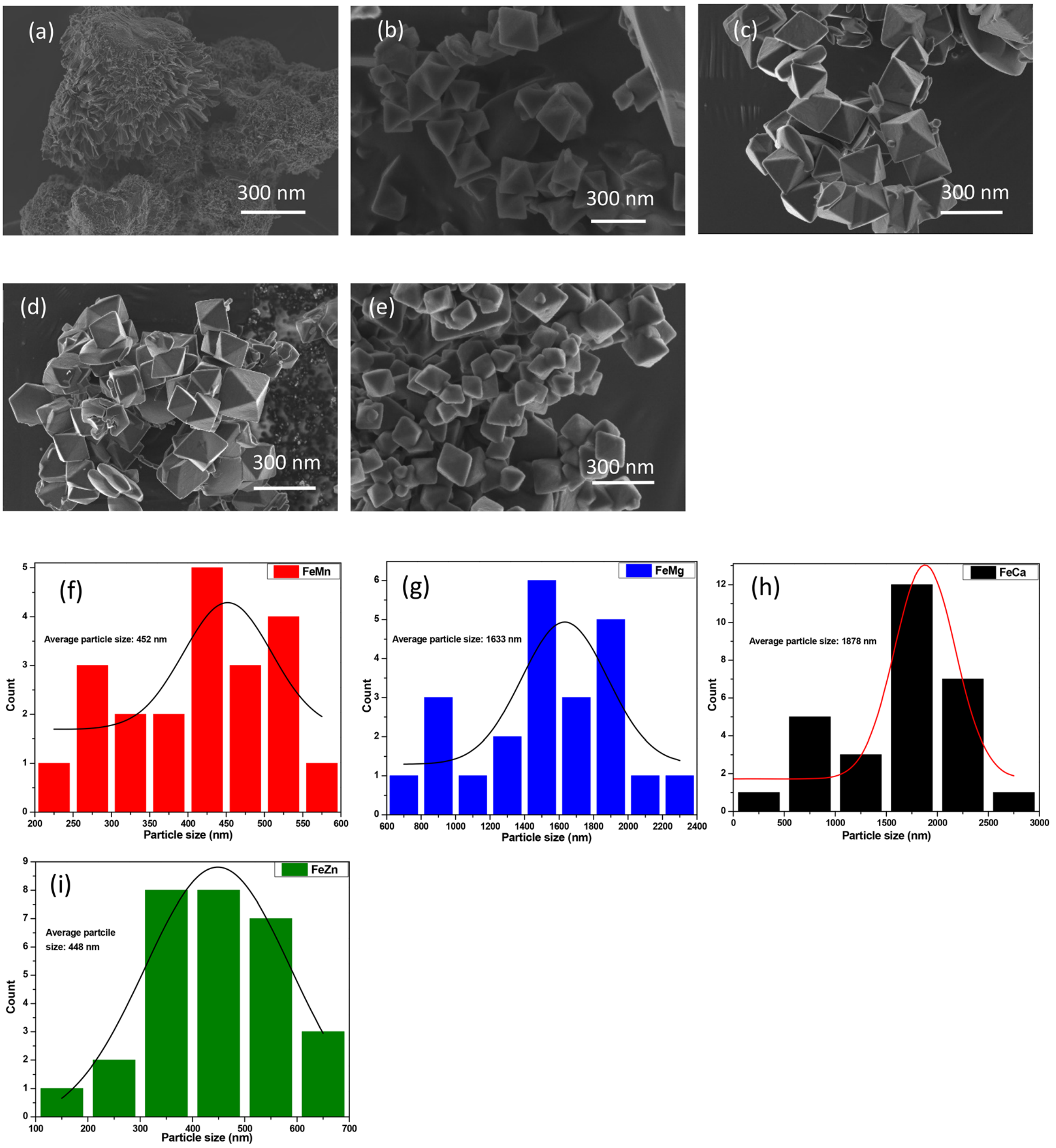

Fig. 4 SEM images of MIL-101 synthesized from bimetallic combinations: (a) FeAl, (b) FeMn, (c) FeMg, (d) FeCa and (e) FeZn, and particle size distribution of (f) FeMn, (g) FeMg, (h) FeCa and (i) FeZn.

weight losses at temperatures below 150 °C. The FeCa-MIL-101 experienced major loss of 25% followed by FeMn-MIL-101 at 18%, while both FeMg-MIL-101 and FeZn-MIL-101 experienced less than 10% mass loss. This could be attributed to the varying solvent/moisture amounts these samples contained. The final mass loss in the temperature range of 300–580 °C is attributed to the breaking down of the MOFs and the degradation of the carboxylate linker, which is similar for all samples. The weight loss at 150 °C for trimetallic combinations also varies. The FeCaMn-MIL-101 sample lost 30% of mass, closely followed by FeAlMg-MIL-101 and FeAlMn-MIL-101 at 25% loss. FeAlCa-MIL-101 lost around 18% mass at a similar temperature. The remaining three samples displayed a weight loss of less than 10% at 150 °C. The prepared structures exhibit high thermal stability, as they have maintained their framework integrity up to 400 °C. The decomposition of the organic linker leads to the collapse of the porous structure and formation of iron oxide particles. The remaining mass for all samples was almost identical, ranging between 25–30%, which is usually observed for Fe-MOFs.

N_2 isotherms and pore size distribution

Fig. 8 displays the N_2 adsorption–desorption of the prepared MIL-101 samples. FeMn-MIL-101 and FeMg-MIL-101 displayed a type I(b), which is associated with porous materials that have a broader pore size distribution range that includes wider

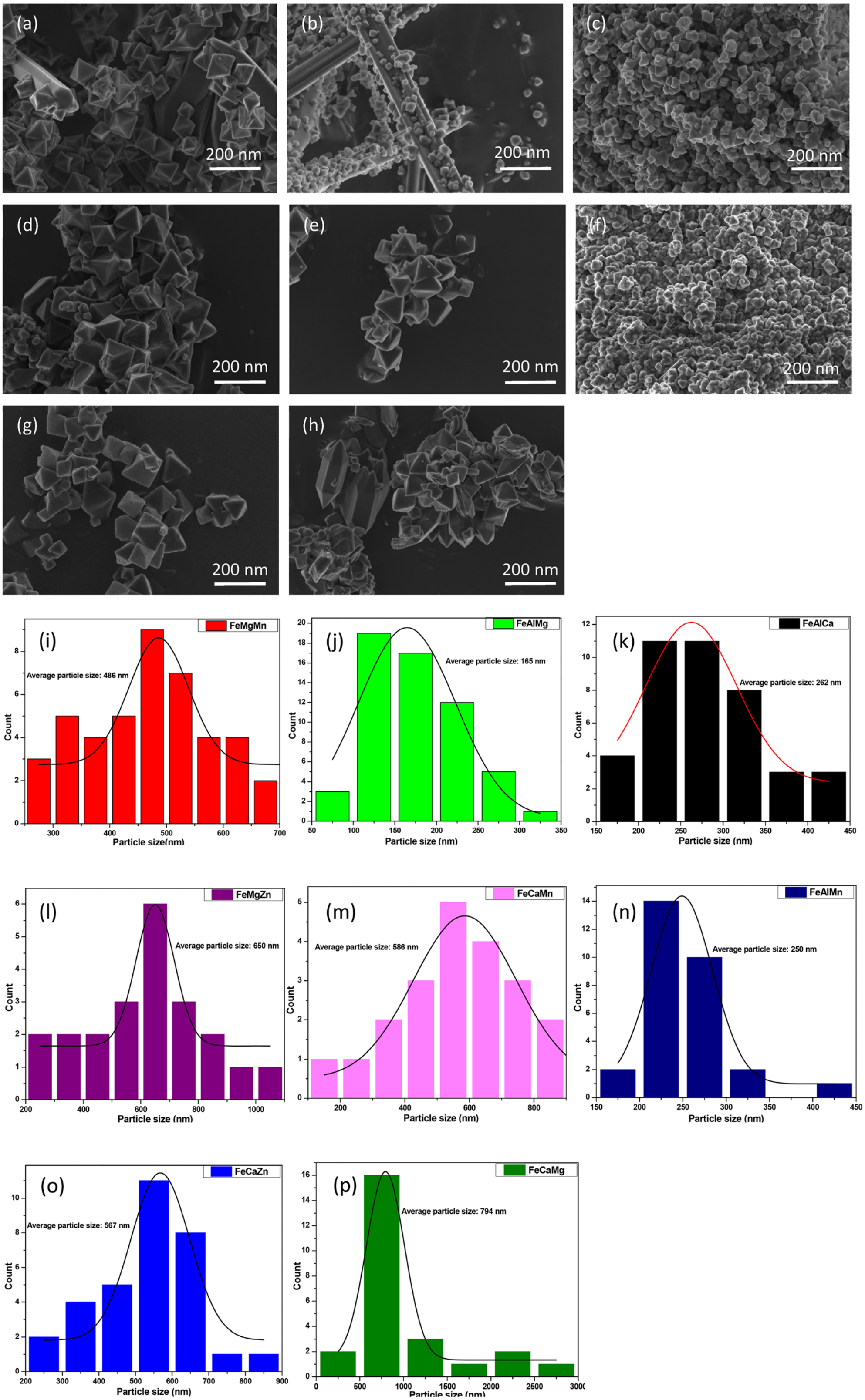

Fig. 5 SEM images of MIL-101 synthesized from trimetallic combinations: (a) FeMgMn, (b) FeAlMg, (c) FeAlCa, (d) FeMgZn, (e) FeCaMn, (f) FeAlMn, (g) FeCaZn and (h) FeCaMg, and particle size distribution of (i) FeMgMn, (j) FeAlMg, (k) FeAlCa, (l) FeMgZn, (m) FeCaMn, (n) FeAlMn, (o) FeCaZn and (p) FeCaMg.

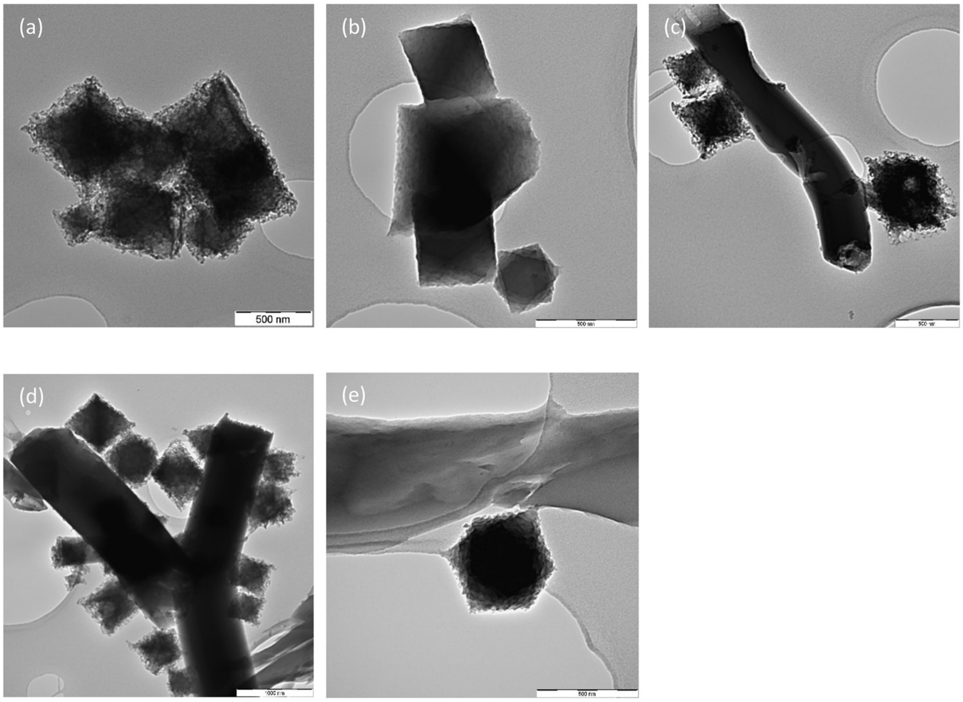

Fig. 6 TEM images of MIL-101 synthesized from (a) FeMn and (b) FeMg bimetallic combinations and (c) FeMgMn, (d) FeAlMg and (e) FeAlCa trimetallic combinations.

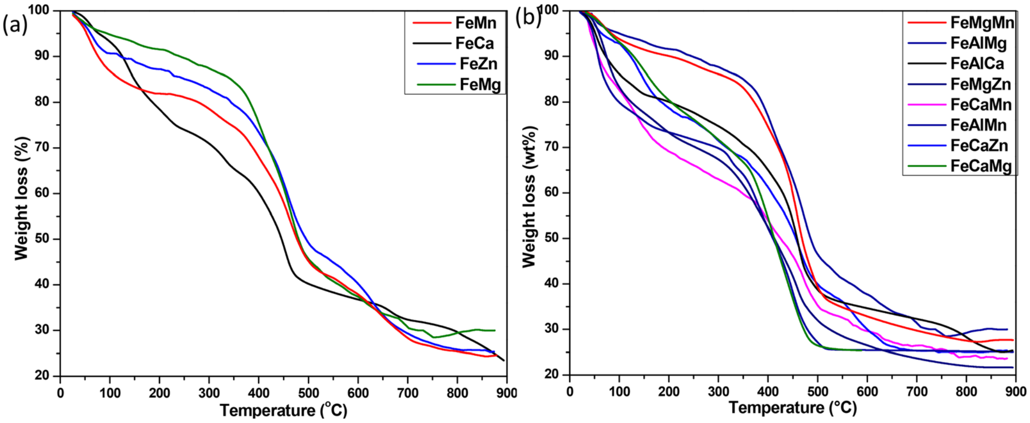

Fig. 7 TGA profiles of MIL-101 synthesized from (a) bimetallic and (b) trimetallic combinations.

micropores and narrow mesopores (<2.5 nm). FeCa-MIL-101 exhibited a combination of type I(b) + IV(a) with hysteresis loop (H4) which might be due to capillary condensation. The steep uptake of N_2 at low relative pressures ($p/p^0 < 0.1$) is indicative of enhanced adsorbate-adsorbent interactions in the narrow micropores. The FeZn-MIL-101 sample displayed a type II behavior (see inset), which is associated with nonporous materials. The trimetallic combination samples exhibited the type I(b) isotherm which is indicative of micro-mesoporous materials. However, the FeCaAl-MIL-101 sample displayed type IV(a) isotherm accompanied by a type H2(b) hysteresis loop. Classification of isotherms and hysteresis loops is well defined by Thommes *et al.*[54]

The specific surface areas calculated using BET method (see Fig. S1 for BET linear plots), and micropore volumes determined using *t*-plot/(Dubinin–Radushkevich) and pore size distributions obtained using the Barrett–Joyner–Halenda (BJH) model assuming cylindrical pores are shown in Table 3. The MIL-101 sample obtained from FeMn combination displayed highest surface area at 2117 m^2 g^{-1} and pore volume of 1.9 cm^3 g^{-1}, followed by samples from FeMg and FeCa combinations at 612 m^2 g^{-1} and 434 m^2 g^{-1} with pore volumes of 0.31 cm^3 g^{-1} and 0.24 cm^3 g^{-1}, respectively. The favorable surface areas of the bimetallic combination encouraged the exploration of the trimetallic combinations. The FeMgMn combination MOF sample displayed a surface area (1438 m^2 g^{-1}) that is

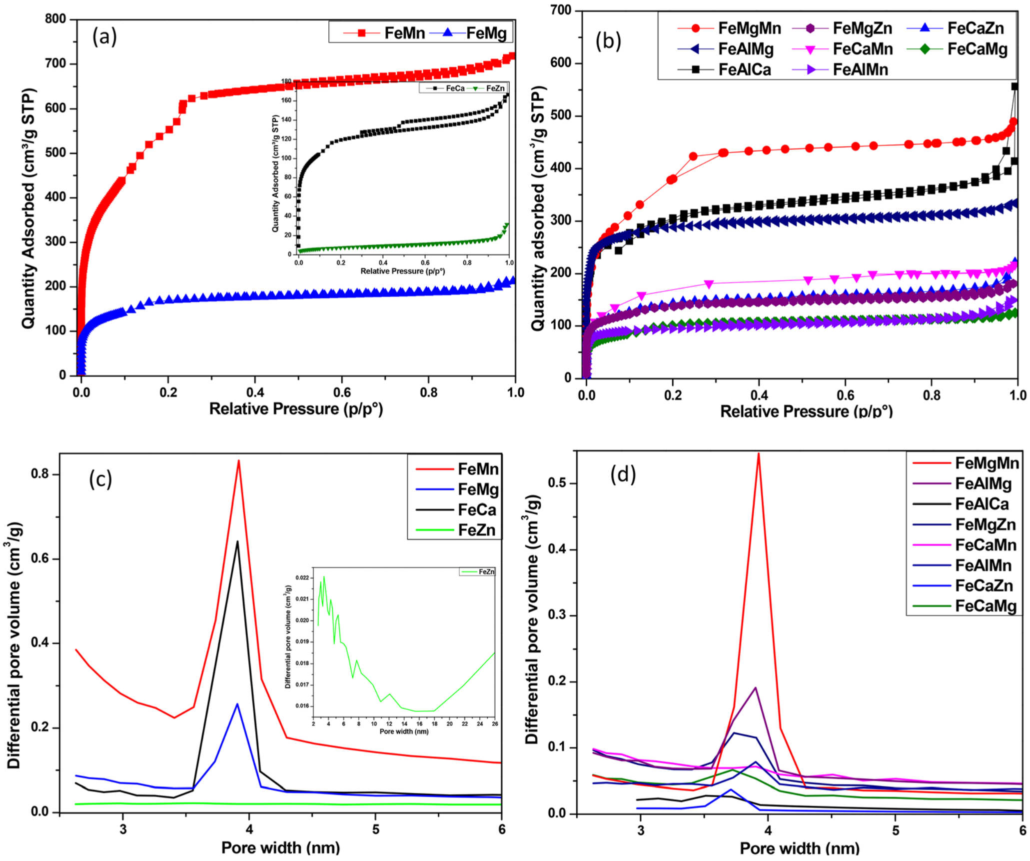

Fig. 8 N_2 sorption isotherms for MIL-101 synthesized from (a) bimetallic and (b) trimetallic combinations; and pore size distribution for MIL-101 synthesized from (c) bimetallic and (d) trimetallic combinations.

Table 3 Textural properties of the prepared MIL-101 samples from bimetallic and trimetallic combinations (DR method micropore volume)

Sample label	A_{BET} ($m^2\ g^{-1}$)	V_{SP} ($cm^3\ g^{-1}$)	V_{micro} ($cm^3\ g^{-1}$)	Average pore width (nm)	H_2 uptake at 77 K, 1 bar (wt%)	CO_2 uptake at 298 K, 20 bar (mmol g^{-1})
FeMn	2120	1.09	0.91 (0. 95)	2.00	1.4	6.2
FeMg	610	0.31	0.25 (0.24)	1.99	0.9	2.4
FeZn	30	0.03	0 (0)	4.40	0	—
FeCa	430	0.24	0.17 (0.19)	2.10	0.8	—
FeMgMn	1440	0.66	0.59 (0.59)	1.70	1.2	4.1
FeMgZn	690	0.3	0.29 (0.33)	1.90	0.8	3.7
FeCaZn	530	0.30	0.18 (0.18)	2.63	0.4	2.8
FeAlMg	1130	0.50	0.43 (0.58)	1.70	1.0	5.3
FeCaMn	500	0.27	0.20 (0.21)	2.00	0.8	2.0
FeCaMg	360	0.18	0.15 (0.15)	2.00	0.7	—
FeAlCa	1120	0.68	0.40 (0.39)	1.54	1.0	5.6
FeAlMn	360	0.21	0.13 (0.17)	2.20	0.8	—

intermediate between that of FeMn-MIL-101 and FeMg-MIL-101 samples. FeAlMg-MIL-101 and FeCaAl-MIL-101 also displayed fairly high surface areas at 1126 $m^2\ g^{-1}$ and 1116 $m^2\ g^{-1}$, respectively. Several other trimetallic combinations with respect to the bimetallic combinations were evaluated and the results are shown in Table 3. The surface area of the remaining samples ranged between 363–692 $m^2\ g^{-1}$ which is low for this MIL type MOF. Although the added metals are not structural, they seem to have an impact on the available surface area and pore volumes. This could be attributed to the possibility of metal ions acting as modulators. Metal ions in solution (although not finally in lattice) can momentarily coordinate with linkers in a similar fashion to modulators. These metals have low lability ($Fe^{3+} < Al^{3+} < Zn^{2+} < Mg^{2+} < Mn^{2+}$) compared to Fe^{3+} which then allows easy ligand exchange.[55] Modulators often affect nucleation rates and growth pathways which may ultimately affect morphology, surface area and pore volume.

The bimetallic combination (FeMn, FeMg and FeCa) displayed the hierarchical nature of MIL-101 where there were pores of size 2.6 nm (narrow mesopores) and 3.9 nm (mesopores) (Fig. 8c).

This pore size distribution agrees with the isotherm types displayed in Fig. 7a. Similarly to bimetallic combinations, trimetallic combinations displayed the bimodal pore nature of MIL-101 (Fig. 8d). The pore size distribution shows that the prepared materials are dominated by mesopores.

Several studies have reported on Fe-MIL-101 with surface areas well above 2000 $m^2 g^{-1}$ and pore volumes above 1.5 $cm^3 g^{-1}$ and bimodal pore size distributions.[31] Only few of the prepared samples exhibited surface areas above 1000 $m^2 g^{-1}$. The low surface areas could be attributed to the mixed morphologies exhibited by some samples (*e.g.*, MOF combination FeMg, FeCaMg and FeMgZn). Fe-MIL-88B is known for its 'breathing effect', which usually affects pore availability and consequently the measured surface area. The presence of irregular and rod-like shapes in the SEM images for samples such as FeCa-MIL-101, FeMgMn-MIL-101 and FeAlMg-MIL-101 (Fig. 4 and 5) are presumed to have affected their surface areas. Cr-MIL-101 is often characterized by high intensity peaks which are indicative of high crystallinity and often result in high surface areas, however, the analogous Fe-MIL-101 tends to display low intensity PXRD peaks and often results in lower surface areas.[56] The PXRD patterns with low intensity peaks observed in of this study shows that the materials are not highly crystalline which has affected their surface areas.

H_2 and CO_2 adsorption

The hydrogen adsorption capacities of the MIL-101 samples were examined at 77 K and 1 bar as shown in Fig. 9a and b. The bimetallic combination MOFs exhibited varying H_2 capacities, but they correspond well with the available pore volumes and surface areas. FeMn-MIL-101 sample displayed the highest capacity of 1.44 wt%, followed by MOF combinations of FeMg and FeCa at 0.88 wt% and 0.77 wt%, respectively. Due to its low surface area FeZn-MIL-101 displayed the lowest H_2 capacity of 0.05 wt%. FeMgMn-MIL-101 displayed H_2 adsorption of 1.22 wt%, closely followed by FeCaAl-MIL-101 at 1.03 wt% and FeAlMg-MIL-101 at 0.97 wt%. The low surface area trimetallic combinations (FeCaZn, FeCaMn, FeCaMg and FeAlMn) displayed H_2 capacities in the range of 0.68–0.79 wt%. These capacities are in line with those reported in the literature for MOFs with similar properties under comparable conditions.[57,58] Higher uptake can be expected for these materials at elevated pressures; this is supported by the lack of saturation in the isotherms at 1 bar. The hierarchical nature of the MOFs can further enhance the adsorption capacity, since mesopores supply additional space (allowing multilayer adsorption), with an increase in pressure. Furthermore, mesopores enhance diffusion rates and encourage spillover from saturated micropores.

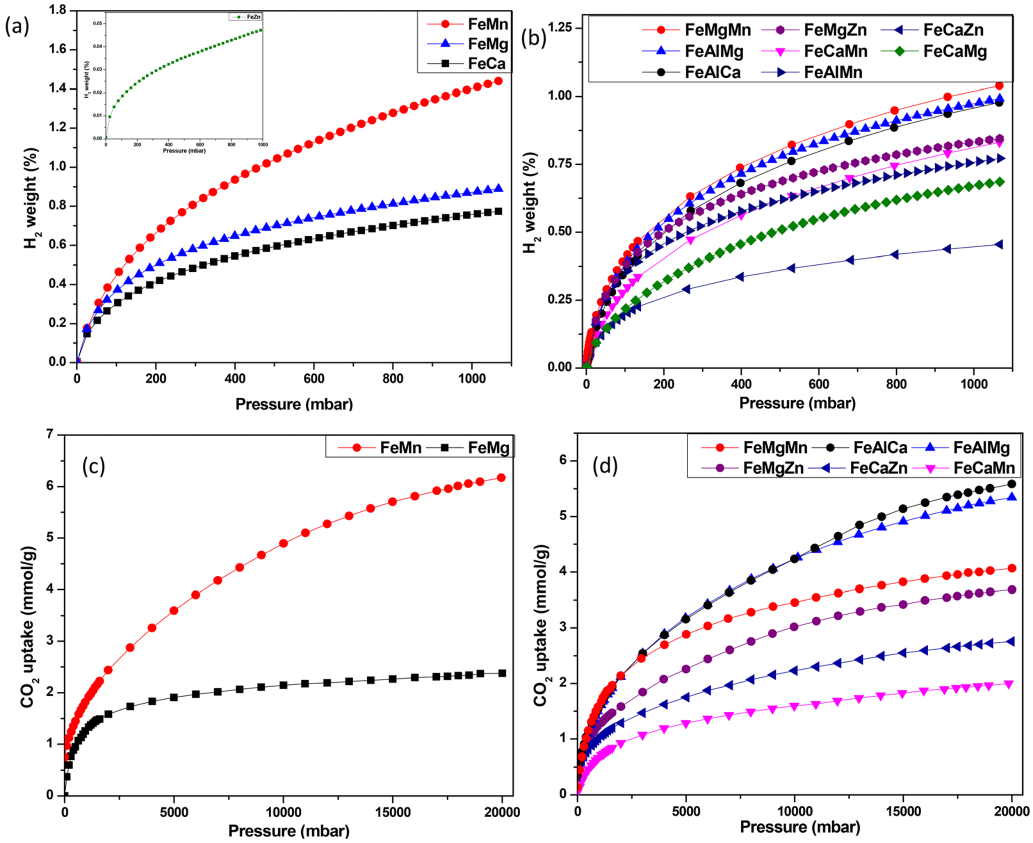

Fig. 9 (a) and (b) Hydrogen uptake for MIL-101 synthesized from bimetallic and trimetallic combinations 77 K at 1 bar; and (c) and (d) carbon dioxide uptake for MIL-101 synthesized from bimetallic and trimetallic combinations at 298 K and 20 bar.

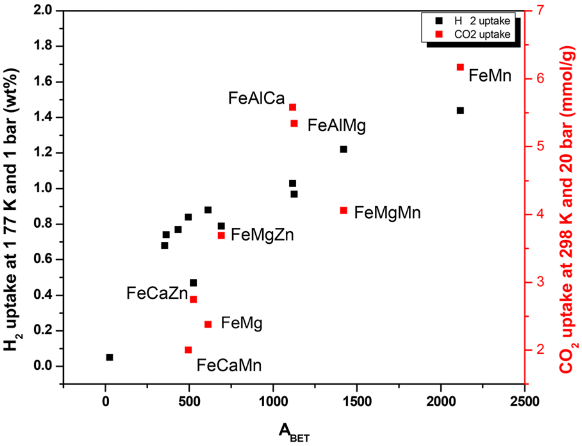

Fig. 10 Correlation between BET surface area and gas (CO_2 and H_2) adsorption capacity.

CO_2 adsorption capacities of selected MIL-101 samples were examined at 298 K and 20 bar as shown in Fig. 8c and d. For porous materials at a high pressure of 20 bar, CO_2 uptake is known to depend on surface area and total pore volume. The relationship between CO_2 uptake and the BET surface area for the prepared MIL-101 samples is shown in Fig. 10. The bimetallic combination of FeMn MOF sample displayed CO_2 adsorption of 6.17 mmol g^{-1}, which corresponds well with the surface area (2117 m^2 g^{-1}). FeMg-MIL-101 exhibited an adsorption of 2.38 mmol g^{-1}, which is low but reasonable for the available surface area (612 m^2 g^{-1}) and pore volume (0.31 cm^3 g^{-1}). For the trimetallic combinations, FeAlCa-MIL-101 and FeAlMg-MIL-101 displayed similar adsorption capacities of 5.58 mmol g^{-1} and 5.34 mmol g^{-1}, respectively. Due to their low surface areas, FeMgZn-MIL-101 and FeCaZn-MIL-101 displayed low adsorption capacities. It has been observed that, when temperature and adsorption pressure are kept constant, materials with higher BET surface area and pore volume exhibit higher CO_2 adsorption capacity. The obtained CO_2 capacities are in line with those reported for other iron-based MOFs.[59,60] But, the iron-based MOFs synthesized here offer the benefit of being derived from Fe-rich waste precursor (AMD) together with PET bottles. The FeMn-MIL-101, with the highest CO_2 adsorption, is particularly promising for pre-combustion CO_2 uptake.

Conclusions

This study presented a possible cost-effective route for the synthesis of iron-based MOFs. The metallic combination displayed promising results for the prepared materials. Majority of the combination resulted in reasonably crystalline materials as confirmed by PXRD. However, the FeAl MOF combination resulted in amorphous material. The prepared samples were mainly dominated by octahedral morphology and trace amounts of trigonal bipyramidal morphology. Irregular and rod-like structures were observed for samples such as FeCa-MIL-101, FeMgMn-MIL-101, FeAlMg-MIL-101. MOF metallic combinations of FeMn, FeMgMn, FeCaAl and FeAlMg displayed surface areas above 1000 m^2 g^{-1} and reasonable H_2 uptakes at 1 bar and 77 K. The highest CO_2 adsorption capacity for the bimetallic combinations was achieved in FeMn-MIL-101 MOF (6.17 mmol g^{-1}), which was influenced by its high available surface area. Trimetallic combination, FeAlCa MOF trailed behind with 5.58 mmol g^{-1}. The CO_2 adsorption of these materials may be improved using functionalized linker to improve electrostatic interactions. It can be concluded that AMD with a high concentration of iron and moderate concentration of other competing metal ions, can be used as an outright precursor for the synthesis of Fe-MOFs. A comprehensive understanding of synergistic interactions between different metal nodes and organic ligands will be beneficial for nucleation, growth and defect-free formation of these MOFs. This will then forge a path towards highly crystalline materials with well-defined pore structures and high surface areas.

Author contributions

K. M.: investigation, methodology, validation, formal analysis, visualization, writing – original draft. C. A. N.: formal analysis, project administration, writing – review & editing. M. M.: resources, writing – review & editing. L. S. B.: investigation, formal analysis, writing – review & editing. R. M.: resources, writing – review & editing. N. M. M.: conceptualization, methodology, funding acquisition, supervision, writing – review & editing. H. W. L.: conceptualization, supervision, funding acquisition, methodology, resources, project administration, writing – review & editing.

Conflicts of interest

There are no conflicts to declare.

Data availability

The data supporting the findings of this study have been included as part of the supplementary information (SI). Supplementary information: adsorption information files for all samples. Linear plots used to determine BET surface area of MIL-101 combinations. Synthesis and characterization of MIL-88B metallic combinations (PXRD, SEM, TGA, BET and H_2 adsorption). See DOI: https://doi.org/10.1039/d6ma00333h.

Acknowledgements

MM and HWL acknowledge funding from MAST3RBoost project funded by the European Union (Call HORIZON-CL4-2021-RESILIENCE-01, Grant Agreement No. 101058574). HWL appreciates Department of Science, Technology and Innovation, and National Research Foundation (NRF) South African Research Chairs Initiative (SARChI, Grant No. 2090155358) as well as NRF CPRR funding instrument (Grant No. 0215586378).

NMM acknowledges financial support from Ningbo Yongjiang Talent Introduction Program (Grant No. 2024A-176-G).

References

1 P. Tholen, Y. Zorlu, J. Beckmann and G. Yücesan, Probing Isoreticular Expansions in phosphonate MOFs and their applications, *Eur. J. Inorg. Chem.*, 2020, (17), 1542–1554.

2 R. Shi, Z. Zhang, F. Yang and C. Zhong, Simultaneously anchoring free carboxyl and sulfonate groups into a metal-organic framework for high proton conductivity, *Microporous Mesoporous Mater.*, 2022, **343**, 112192.

3 P. Kukkar, K.-H. Kim, D. Kukkar and P. Singh, Recent advances in the synthesis techniques for zeolitic imidazolate frameworks and their sensing applications, *Coord. Chem. Rev.*, 2021, **446**, 214109.

4 H. Sun, Z. Chen, J. Zhou, L. Chen and W. Zuo, Recovery of high-quality terephthalic acid from waste polyester textiles via a neutral hydrolysis method, *J. Environ. Chem. Eng.*, 2024, **12**(3), 112558.

5 A. K. Nason, R. T. Jerozal, P. J. Milner and J. Suntivich, Reactive crystallization via metal–organic-framework formation enables separation of terephthalic acid from textile impurities, *ACS Sustainable Chem. Eng.*, 2022, **11**(1), 18–22.

6 M. Wang, K. Liu, Z. Xu, S. Dutta, M. Valix, D. S. Alessi, L. Huang, J. B. Zimmerman and D. C. Tsang, Selective extraction of critical metals from spent lithium-ion batteries, *Environ. Sci. Technol.*, 2023, **57**(9), 3940–3950.

7 J. Qing, X. Wu, L. Zeng, W. Guan, Z. Cao, Q. Li, M. Wang, G. Zhang and S. Wu, Novel approach to recycling of valuable metals from spent lithium-ion batteries using hydrometallurgy, focused on preferential extraction of lithium, *J. Cleaner Prod.*, 2023, **431**, 139645.

8 K. M. Rambau, N. M. Musyoka, R. Panek, W. Franus, M. Wdowin and N. Manyala, Preparation of coal fly ash derived metal organic frameworks and their carbon derivatives, *Mater. Today Commun.*, 2021, **27**, 102433.

9 K. Mosupi, M. Masukume, G. Weng, N. M. Musyoka and H. W. Langmi, Recent advances in Fe-based metal-organic frameworks: Structural features, synthetic strategies and applications, *Coord. Chem. Rev.*, 2025, **529**, 216467.

10 K. Mosupi, N. T. Mthembu, M. Masukume, N. M. Musyoka and H. W. Langmi, Synthesis of iron-based metal–organic frameworks and carbon derivatives via unconventional synthetic methods and waste precursors with potential for gas storage, *Mater. Adv.*, 2025, **6**, 9806–9816.

11 D. K. Nordstrom, Mine waters: acidic to circmneutral, *Elements*, 2011, **7**(6), 393–398.

12 V. M. Ngole-Jeme and J. Ndava, The implications of AMD induced acidity, high metal concentrations and ochre precipitation on aquatic organisms, *Pol. J. Environ. Stud.*, 2023, **32**(4), 2959.

13 J. Yuan, Z. Ding, Y. Bi, J. Li, S. Wen and S. Bai, Resource utilization of acid mine drainage (AMD): A review, *Water*, 2022, **14**(15), 2385.

14 Q. Yan, Z. Yang and Z. Chen, Recent advances in microbial nanomaterials/nanoparticles synthesis and rare earth elements recovery from rare earth mine wastewater: A review, *Chem. Eng. J.*, 2025, 161647.

15 M. K. Agusta, A. G. Saputro, V. V. Tanuwijaya, N. N. Hidayat and H. K. Dipojono, Hydrogen adsorption on Fe-based metal organic frameworks: DFT study, *Procedia Eng.*, 2017, **170**, 136–140.

16 M. Dincă and J. R. Long, Hydrogen storage in microporous metal–organic frameworks with exposed metal sites, *Angew. Chem., Int. Ed.*, 2008, **47**(36), 6766–6779.

17 J. G. Vitillo, L. Regli, S. Chavan, G. Ricchiardi, G. Spoto, P. D. Dietzel, S. Bordiga and A. Zecchina, Role of exposed metal sites in hydrogen storage in MOFs, *J. Am. Chem. Soc.*, 2008, **130**(26), 8386–8396.

18 Z. Yu, M. Lepoitevin and C. Serre, Iron-MOFs for biomedical applications, *Adv. Healthcare Mater.*, 2025, **14**(8), 2402630.

19 X. Dyosiba, J. Ren, N. M. Musyoka, H. W. Langmi, M. Mathe and M. S. Onyango, Preparation of value-added metal-organic frameworks (MOFs) using waste PET bottles as source of acid linker, *Sustainable Mater. Technol.*, 2016, **10**, 10–13.

20 T. Kulandaivel, A. Subhramaniyan Rasappan, K. Venkatesan Savunthari, M. S. Samuel, M. Kumar, H.-U. Dahms, A. K. Anbalagan, G. Mohan, S. Kheawhom and S. Ganesan, Facile fabrication of amorphous Al/Fe based metal–organic framework as effective heterogeneous fenton catalyst for environmental remediation, *Environ. Geochem. Health*, 2024, **46**(5), 156.

21 T. D. Bennett and S. Horike, Liquid, glass and amorphous solid states of coordination polymers and metal–organic frameworks, *Nat. Rev. Mater.*, 2018, **3**(11), 431–440.

22 H. Yin, K. D. Kwon, J.-Y. Lee, Y. Shen, H. Zhao, X. Wang, F. Liu, J. Zhang and X. Feng, Distinct effects of Al^{3+} doping on the structure and properties of hexagonal turbostratic birnessite: A comparison with Fe^{3+} doping, *Geochim. Cosmochim. Acta*, 2017, **208**, 268–284.

23 I. Bechis, A. F. Sapnik, A. Tarzia, E. H. Wolpert, M. A. Addicoat, D. A. Keen, T. D. Bennett and K. E. Jelfs, Modeling the effect of defects and disorder in amorphous metal–organic frameworks, *Chem. Mater.*, 2022, **34**(20), 9042–9054.

24 S. Dissegna, K. Epp, W. R. Heinz, G. Kieslich and R. A. Fischer, Defective metal-organic frameworks, *Adv. Mater.*, 2018, **30**(37), 1704501.

25 Y. Liu, P. Gao, C. Huang and Y. Li, Shape-and size-dependent catalysis activities of iron-terephthalic acid metal-organic frameworks, *Sci. China: Chem.*, 2015, **58**(10), 1553–1560.

26 T. Tanasaro, K. Adpakpang, S. Ittisanronnachai, K. Faungnawakij, T. Butburee, S. Wannapaiboon, M. Ogawa and S. Bureekaew, Control of polymorphism of metal–organic frameworks using mixed-metal approach, *Cryst. Growth Des.*, 2018, **18**(1), 16–21.

27 Q. Wu, M. S. Siddique, Y. Guo, M. Wu, Y. Yang and H. Yang, Low-crystalline bimetallic metal-organic frameworks as an excellent platform for photo-Fenton degradation of organic

contaminants: Intensified synergism between hetero-metal nodes, *Appl. Catal., B*, 2021, **286**, 119950.

28 Q. Sun, M. Liu, K. Li, Y. Han, Y. Zuo, F. Chai, C. Song, G. Zhang and X. Guo, Synthesis of Fe/M (M= Mn, Co, Ni) bimetallic metal organic frameworks and their catalytic activity for phenol degradation under mild conditions, *Inorg. Chem. Front.*, 2017, **4**(1), 144–153.

29 H. R. Abid, H. Znad, N. M. Alawi, F. L. Rashid, A. Dulaimi, A. Alanazi, A. Keshavarz, S. Iglauer and S. Wang, Enhancing CO_2 adsorption and CO_2/N_2 separation performance by incorporating calcium in MIL-53 (Al), *Int. J. Environ. Res.*, 2026, **20**(2), 97.

30 T. A. Vu, G. H. Le, C. D. Dao, L. Q. Dang, K. T. Nguyen, P. T. Dang, H. T. Tran, Q. T. Duong, T. V. Nguyen and G. D. Lee, Isomorphous substitution of Cr by Fe in MIL-101 framework and its application as a novel heterogeneous photo-Fenton catalyst for reactive dye degradation, *RSC Adv.*, 2014, **4**(78), 41185–41194.

31 C. Gecgel, U. B. Simsek, B. Gozmen and M. Turabik, Comparison of MIL-101 (Fe) and amine-functionalized MIL-101 (Fe) as photocatalysts for the removal of imidacloprid in aqueous solution, *J. Iran. Chem. Soc.*, 2019, **16**(8), 1735–1748.

32 T. Tian, J. Zhang, S. Ge and L. Tian, Enhanced gaseous benzene degradation by bimetallic MIL-101 (Fe, Cu) activated persulfate system: Efficiency and mechanism, *Colloids Surf., A*, 2025, **706**, 135785.

33 A. Sun, J. Lu, T. Liu, C. Feng, Y. Liu, J. Pang, L. Chen, Z. Wu, S. Han and Z. Li, Characterization and mechanism of action of bimetallic-modified MIL-101 (Fe) magnetic composites for enhanced removal of polystyrene from water, *Sep. Purif. Technol.*, 2025, 133397.

34 M.-J. Duan, Z.-y Guan, Y.-W. Ma, J.-Q. Wan, Y. Wang and Y.-F. Qu, A novel catalyst of MIL-101 (Fe) doped with Co and Cu as persulfate activator: synthesis, characterization, and catalytic performance, *Chem. Pap.*, 2018, **72**(1), 235–250.

35 Y. Luo, X. Yang, L. He, Y. Zheng, J. Pang, L. Wang, R. Jiang, J. Hou, X. Guo and L. Chen, Structural and electronic modulation of iron-based bimetallic metal–organic framework bifunctional electrocatalysts for efficient overall water splitting in alkaline and seawater environment, *ACS Appl. Mater. Interfaces*, 2022, **14**(41), 46374–46385.

36 J. Zhang, Y. Zhao, W. Zhao, J. Wang, Y. Hu, C. Huang, X. Zou, Y. Liu, D. Zhang and X. Lu, Improving electrocatalytic oxygen evolution through local field distortion in Mg/Fe dual-site catalysts, *Angew. Chem., Int. Ed.*, 2023, **62**(52), e202314303.

37 R. M. Main, D. B. Cordes, A. V. Desai, A. M. Slawin, P. Wheatley, A. R. Armstrong and R. E. Morris, Solvothermal synthesis of a novel calcium metal-organic framework: High temperature and electrochemical behaviour, *Molecules*, 2021, **26**(22), 7048.

38 C. Castillo-Blas, N. López-Salas, M. C. Gutiérrez, I. Puente-Orench, E. Gutiérrez-Puebla, M. L. Ferrer, M. Á. Monge and F. Gándara, Encoding metal–cation arrangements in metal–organic frameworks for programming the composition of electrocatalytically active multimetal oxides, *J. Am. Chem. Soc.*, 2019, **141**(4), 1766–1774.

39 X. Yang and Q. Xu, Bimetallic metal–organic frameworks for gas storage and separation, *Cryst. Growth Des.*, 2017, **17**(4), 1450–1455.

40 A. Arenas-Vivo, D. Avila and P. Horcajada, Phase-selective microwave assisted synthesis of iron(III) aminoterephthalate MOFs, *Materials*, 2020, **13**(6), 1469.

41 F. Carson, J. Su, A. E. Platero-Prats, W. Wan, Y. Yun, L. Samain and X. Zou, Framework isomerism in vanadium metal–organic frameworks: MIL-88B (V) and MIL-101 (V), *Cryst. Growth Des.*, 2013, **13**(11), 5036–5044.

42 S. Bauer, C. Serre, T. Devic, P. Horcajada, J. Marrot, G. Férey and N. Stock, High-throughput assisted rationalization of the formation of metal organic frameworks in the iron(III) aminoterephthalate solvothermal system, *Inorg. Chem.*, 2008, **47**(17), 7568–7576.

43 A. D. Barbosa, D. Julião, D. M. Fernandes, A. F. Peixoto, C. Freire, B. de Castro, C. M. Granadeiro, S. S. Balula and L. Cunha-Silva, Catalytic performance and electrochemical behaviour of Metal–organic frameworks: MIL-101 (Fe) versus NH_2-MIL-101 (Fe), *Polyhedron*, 2017, **127**, 464–470.

44 H. Hu, H. Zhang, Y. Chen, Y. Chen, L. Zhuang and H. Ou, Enhanced photocatalysis degradation of organophosphorus flame retardant using MIL-101 (Fe)/persulfate: effect of irradiation wavelength and real water matrixes, *Chem. Eng. J.*, 2019, **368**, 273–284.

45 Z. Li, X. Liu, W. Jin, Q. Hu and Y. Zhao, Adsorption behavior of arsenicals on MIL-101 (Fe): the role of arsenic chemical structures, *J. Colloid Interface Sci.*, 2019, **554**, 692–704.

46 K. Mosupi, C. A. Ndamyabera, M. Masukume, N. M. Musyoka and H. W. Langmi, Facile Synthesis of Iron-Based MIL-101 Metal-Organic Framework as a Potential Hydrogen Storage Material, *J. Inorg. Organomet. Polym. Mater.*, 2026, 1–11.

47 S. H. Ghoochani, A. Heshmati, H. A. Hosseini and M. Darroudi, Adsorption and photocatalytic properties of porphyrin loaded MIL-101 (Cr) in methylene blue degradation, *Environ. Sci. Pollut. Res.*, 2022, **29**(23), 34406–34418.

48 R. Tang, K. Xing, J. Tu, X. Wang, L. Xu, W. Chen, Y. Cheng and Z. Xu, Application and Cytotoxicity Evaluation of Fe-MIL-101 Nanozyme in Milk, *Appl. Biochem. Biotechnol.*, 2025, **197**(1), 482–496.

49 C. R. Marshall, S. A. Staudhammer and C. K. Brozek, Size control over metal–organic framework porous nanocrystals, *Chem. Sci.*, 2019, **10**(41), 9396–9408.

50 E. Haque and S. H. Jhung, Synthesis of isostructural metal–organic frameworks, CPO-27s, with ultrasound, microwave, and conventional heating: Effect of synthesis methods and metal ions, *Chem. Eng. J.*, 2011, **173**(3), 866–872.

51 S. Singh, D. Bhatt, A. Deep and U. K. Tiwari, An antibody conjugated NH_2-MIL-101 (Fe) metal-organic framework based optical biosensor for sensitive detection of lead ions, *Microchem. J.*, 2024, **199**, 110122.

52 J.-M. Yang, R.-Z. Zhang and Y.-Y. Liu, Superior adsorptive removal of anionic dyes by MIL-101 analogues: the effect of

free carboxylic acid groups in the pore channels, *CrystEngComm*, 2019, **21**(38), 5824–5833.

53 M. Zou, M. Dong, M. Luo, H. Zhu and T. Zhao, Nanofused hierarchically porous MIL-101 (Cr) for enhanced methyl orange removal and improved catalytic activity, *Materials*, 2022, **15**(10), 3645.

54 M. Thommes, K. Kaneko, A. V. Neimark, J. P. Olivier, F. Rodriguez-Reinoso, J. Rouquerol and K. S. Sing, Physisorption of gases, with special reference to the evaluation of surface area and pore size distribution (IUPAC Technical Report), *Pure Appl. Chem.*, 2015, **87**(9–10), 1051–1069.

55 E. Haque, J. H. Jeong and S. H. Jhung, Synthesis of isostructural porous metal-benzenedicarboxylates: Effect of metal ions on the kinetics of synthesis, *CrystEngComm*, 2010, **12**(10), 2749–2754.

56 H. T. M. Thanh, T. T. T. Phuong, P. T. Le Hang, T. T. T. Toan, T. N. Tuyen, T. X. Mau and D. Q. Khieu, Comparative study of Pb(II) adsorption onto MIL–101 and Fe–MIL–101 from aqueous solutions, *J. Environ. Chem. Eng.*, 2018, **6**(4), 4093–4102.

57 A. M. P. Peedikakkal and I. H. Aljundi, Upgrading the hydrogen storage of MOF-5 by post-synthetic exchange with divalent metal ions, *Appl. Sci.*, 2021, **11**(24), 11687.

58 D. Yuan, D. Zhao, D. Sun and H. C. Zhou, An isoreticular series of metal–organic frameworks with dendritic hexacarboxylate ligands and exceptionally high gas-uptake capacity, *Angew. Chem.*, 2010, **122**(31), 5485–5489.

59 H. R. Mahdipoor, R. Halladj, E. G. Babakhani, S. Amjad-Iranagh and J. S. Ahari, Synthesis, characterization, and CO_2 adsorption properties of metal organic framework Fe-BDC, *RSC Adv.*, 2021, **11**(9), 5192–5203.

60 H. R. Mahdipoor, R. Halladj, E. G. Babakhani, S. Amjad-Iranagh and J. S. Ahari, Adsorption of CO_2, N_2 and CH_4 on a Fe-based metal organic framework, MIL-101 (Fe)–NH_2, *Colloids Surf., A*, 2021, **619**, 126554.